Journal of
Composites Science

MDPI

Article

Microstructural Evaluation and Fracture Behavior of AZ31/Nb_2O_5 Metal Matrix Composite

Song-Jeng Huang, Manas Sarkar and Sathiyalingam Kannaiyan *

Department of Mechanical Engineering, National Taiwan University of Science and Technology, Taipei 106, Taiwan
* Correspondence: sathiaerospace@gmail.com

Abstract: There have been remarkable improvements in the research field of magnesium over the last few decades, especially in the magnesium metal matrix composite in which micro and nanoparticles are used as reinforcement. The dispersion phase of nanoparticles shows a better microstructural morphology than pure magnesium. The magnesium metal matrix nanocomposite shows improved strength with a balance of plasticity as compared to the traditional magnesium metal matrix composite. In this research, Nb_2O_5 (0 wt.%, 3 wt.%, and 6 wt.%) nanoparticles were used to reinforce AZ31 with the stir casting method, followed by heat treatment, and finally, an investigation was conducted using microstructural analysis. Factors such as the degree of crystallinity, crystallite size, and dislocation density are affected by the concentration of Nb_2O_5 and heat treatment. With the compositional increase in Nb_2O_5 weight percentage, the grain size decreases up to 3% Nb_2O_5 and then increases gradually. The SEM image analysis showed a grain size reduction of up to 3% Nb_2O_5 and fracture morphology changed from basal slip to a mixture of basal slip and adiabatic shear band.

Keywords: metal matrix composite; AZ31 alloy; stir casting; microstructure; fracture studies

Citation: Huang, S.-J.; Sarkar, M.; Kannaiyan, S. Microstructural Evaluation and Fracture Behavior of AZ31/Nb_2O_5 Metal Matrix Composite. *J. Compos. Sci.* **2022**, *6*, 390. https://doi.org/10.3390/jcs6120390

Academic Editor: Prashanth Konda Gokuldoss

Received: 19 October 2022
Accepted: 8 December 2022
Published: 14 December 2022

1. Introduction

Attention towards carbon emissions has been taken very seriously over the last decade, especially the carbon emissions produced by automobiles and some major manufacturing industries. Research on weight reduction could be a solution to carbon emission reduction [1–3]. With two-thirds the density of aluminum, the use of magnesium instead of aluminum can reduce carbon dioxide and carbon monoxide, as well as other unburnt residuals from fossil fuel. The concerning factor about magnesium is its strength and fracture behavior. Due to less creep and corrosion resistance, the use of magnesium is still lesser than aluminum [4]. The required improvement in strength can be achieved by reinforcement of the pure alloys, followed by heat treatment, coldwork, etc., and further followed by severe plastic deformation [4–8].

The fabrication method used to fabricate the composite was stir casting because of its availability, cost-effectiveness, and large-scale casting capacity [8–11]. The addition of reinforcement helps to distribute the secondary phase evenly along the matrix material and the agglomeration of aluminum can be reduced [8]. As reported by J. Zhu et al., the addition of Nb_2O_5 in TiAl composite increases its flexural strength and fracture toughness tremendously [12]. As we focused on the mechanical strengthening of AZ31 with a certain percentage of Nb_2O_5, the choice of Nb_2O_5 (reinforcement) depends on its properties, as well as its application. The properties of Nb_2O_5 include excellent thermal, chemical, and thermodynamic stability, high reflective indices, excellent mechanical properties, and excellent fracture toughness. The superior catalytic property of Nb_2O_5 enabled hydrogen absorption and desorption, along with biomedical and sensor applications [13]. Nb_2O_5 has not yet been fully explored in terms of its potential benefits and applications. Due to their low wear resistance, low hardness, and low malleability, Mg–Zn alloys have some disadvantages that limit their use. Nb_2O_5 as a reinforcement helps to overcome the limitation in the magnesium matrix composite. In the selected matrix, Nb_2O_5 reinforcement is added by the stir casting method. To verify the phase composition of the fabricated composite, XRD analyses were performed. Microstructural characterization was done by SEM image analyses and EDS to verify the elemental distribution in the composite. Mechanical testing, such as compression and microhardness, was performed, and the broken specimen surface was analyzed by SEM to understand the fracture mechanics.

2. Materials and Methods

The magnesium alloy AZ31 was used as a base material for the metal matrix composite (MMC), which consists of Al-5.95, Zn-0.64, Mn-0.26, Fe-0.005, Si-0.009, Cu-0.0008, Ni-0.0007, and Mg balance. The dispersion reinforcement used in these MMCs was an oxide called Nb_2O_5 with a particle size of 100 nm diameter. Various weight percentage of Nb_2O_5 was used and mentioned in Table 1. Figure 1 shows the method of the experiment in which stir casting was used to fabricate the AZ31/ Nb_2O_5 metal matrix composite based on the casting feasibility. During casting, at every 100 °C increase in temperature, a stabilization time of 15 min was given up to 700 °C and when the temperature crossed 760 °C, the final stabilization time of 30 min was given and the molten alloy was stirred for 5 min at 300 rpm to distribute the nanoparticles equally in the MMCs. Carbon dioxide (CO_2) and sulfur hexafluoride (SF_6) gases were used at 400 °C to avoid magnesium burning, and at 700 °C, argon gas was used to avoid oxidation. The molten mixed MMCs were then poured into a crucible under the furnace. The casted ingots were taken for billet cutting. Some sets of billets with various compositions of Nb_2O_5 were taken to examine the microstructural evaluation. In order to examine the microstructure, mechanical grinding and polishing procedures were followed. The samples were polished and then etched with 100 mL of ethanol, 10 mL of DI water, 5 mL of acetic acid, and 6 g of the picric acid solution for 40 s before being taken for microstructure evaluation. SEM images were taken with the JSM-6500F machine and XRD (Bruker D2 phaser model) was used to confirm the phase intensity and planes. The grain size was calculated using the ImageJ (version 1.53v21, Bethesda, MD, USA) analysis software. The formula used to calculate the parameters like dislocation density and microstrain are given below:

Table 1. Composition of AZ31 and reinforcement.

Types of Cast Ingots	Nb_2O_5 wt.%	Nb_2O_5 Size (nm)
Pure AZ31	0	-
Nb_2O_5/AZ31	3	100
Nb_2O_5/AZ31	6	100

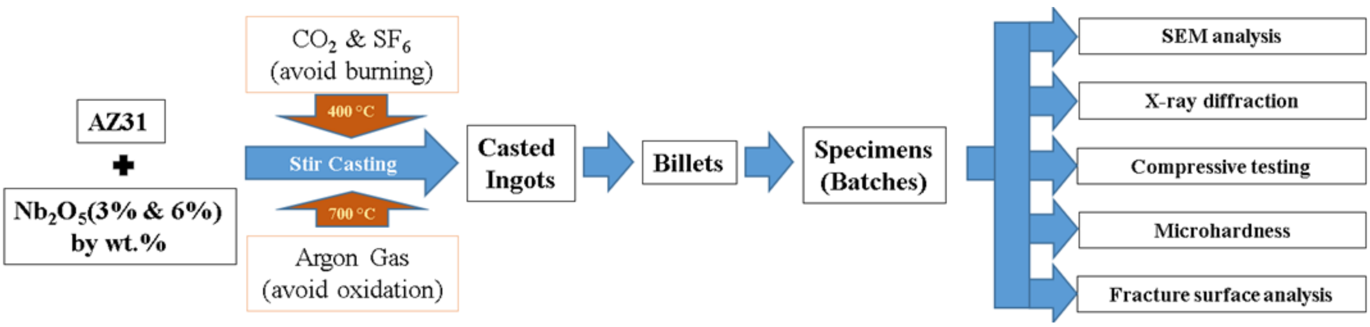

Figure 1. Schematic of Experimental Methodology.

(i) Crystallite diameter (D) = $k\lambda/\beta \cos\theta$
(ii) Dislocation Density (δ) = $1/D^2$
(iii) Microstrain (ε) = $\beta/(4 \tan\theta)$

where β—values corresponding to FWHM value (Full width at half maximum) of XRD profile, k—Shape factor (0.89), λ—Wavelength of XRD radiation, θ—peak position.

The specimen sets were cut for the compression test according to ASTM E9-19, and the UTM-100 machine was used to perform the test. The tested specimens were taken for scan-electron microscopy (SEM) image analysis to analyze the fracture surface.

3. Results & Discussion

3.1. Microstructural Evaluation

3.1.1. SEM Image Analysis

The SEM images shows the grain morphology and the EDS shows the elemental distribution in the casted AZ31 composite showed in Figure 2. The EDS images reveal the proper distribution of magnesium throughout the grain, but the agglomeration of aluminum around the grain boundary and also the presence of magnesium in the grain boundary indicate the formation of the $Mg_{17}Al_{12}$ secondary phase. Figure 2d shows the even distribution of Zn along the matrix, which contributes to a single-phase $Al_5Mg_{11}Zn_4$.

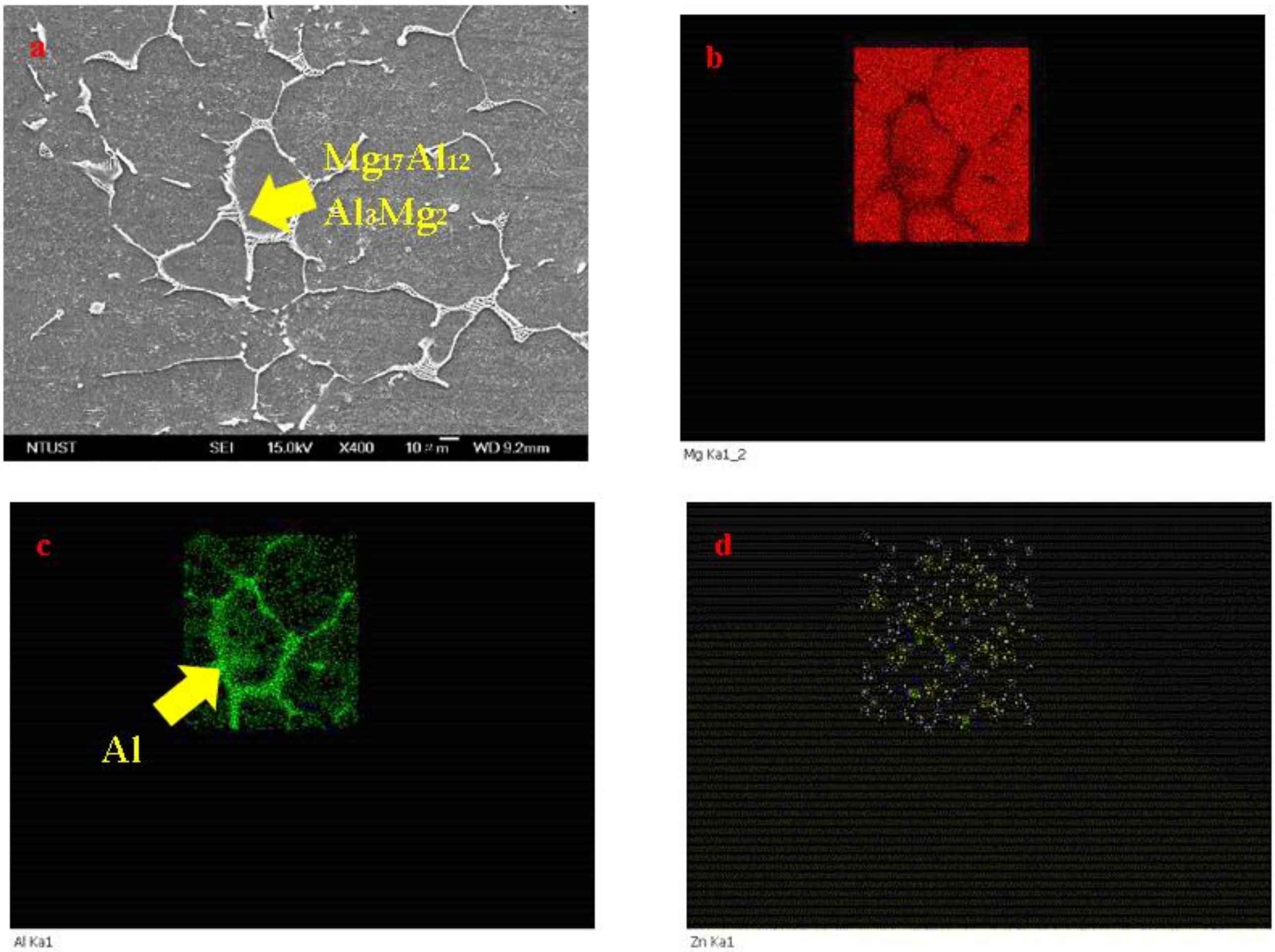

Figure 2. (**a**) SEM of AZ31 microstructure, (**b**) EDS shows Mg distribution, (**c**) EDS shows Al distribution, and (**d**) EDS shows Nb distribution.

The EDS images in Figure 3b,d–f correspond to Mg, Zn, Nb, and O with a proper distribution; however (c) represents Al, which combines with Mg, resulting in the formation of the secondary phase. The secondary phase ($Mg_{17}Al_{12}$) of 3% Nb_2O_5 + AZ31 exhibited a 12.5% lower intensity as compared to the pure as-cast AZ31 composite, and the secondary phase Al_3Mg_2 of 3% Nb_2O_5 + AZ31 exhibited a 30.6% lower intensity compared to pure as-cast AZ31 composite. Hence, it is self-explanatory that the addition of 3% Nb_2O_5

restricted the formation of the Al_3Mg_2, $Mg_{17}Al_{12}$ phase. The phase quantification is shown in Table 2. The flax can be seen in the figure, but there is a very minute trace of aluminum in it, so the denser oxygen presence and niobium formed $Mg_4Nb_2O_9$. The secondary phase is distributed unevenly and is more discontinuous and separated. The dispersion of aluminum in Figure 2c is greater compared to Figure 3c, which shows the broadness of the grain boundary of Figure 2a compared to Figure 3a and that the change in microstructure and broadness of grain boundary took place due to the added reinforcement i.e., 3% Nb_2O_5 + AZ31.

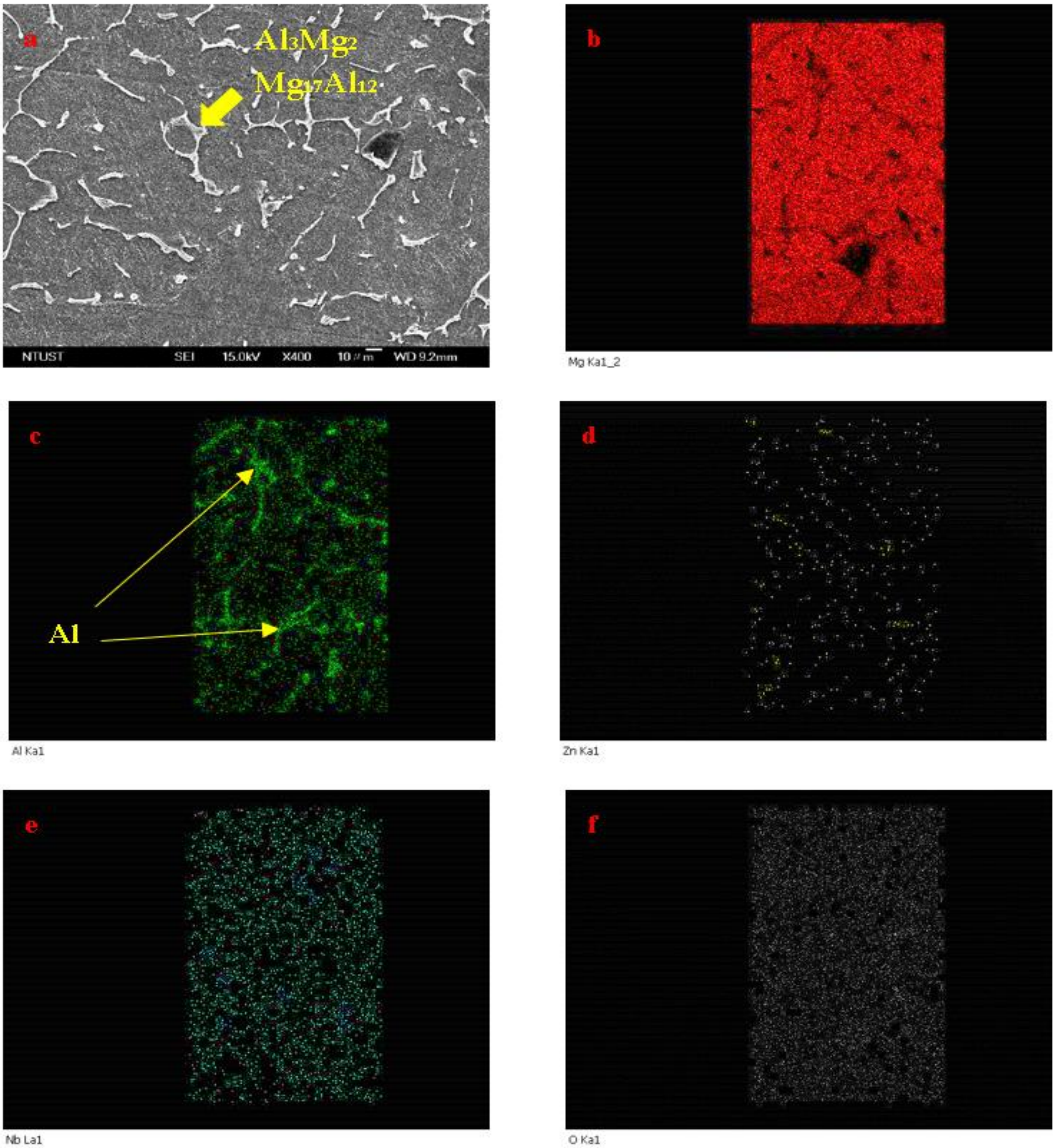

Figure 3. (**a**) SEM of 3% Nb_2O_5 + AZ31 microstructure, (**b**) EDS shows Mg distribution, (**c**) EDS shows Al distribution, (**d**) EDS shows Zn distribution, (**e**) EDS shows Nb distribution, (**f**) EDS shows O distribution.

Table 2. Shows phase quantification and crystal structure.

Phase Quantification			
Composition (wt.%)	**Major Phase**	**Crystal Structure**	**Percentage**
AZ31	Mg	Hexagonal	25.6
	$Al_{12}Mg_{17}$	Cubic	0.8
	Al_3Mg_2	Cubic	6.2
	$Al_5Mg_{11}Zn_4$	Orthorhombic	67.4
	$Mg_4Nb_2O_9$	Hexagonal	0
3% Nb_2O_5/AZ31	Mg	Hexagonal	20
	$Al_{12}Mg_{17}$	Cubic	0.6
	Al_3Mg_2	Cubic	4.3
	$Al_5Mg_{11}Zn_4$	Orthorhombic	52.9
	$Mg_4Nb_2O_9$	Hexagonal	22.1
6% Nb_2O_5/AZ31	Mg	Hexagonal	19.4
	$Al_{12}Mg_{17}$	Cubic	0.5
	Al_3Mg_2	Cubic	5.6
	$Al_5Mg_{11}Zn_4$	Orthorhombic	51.8
	$Mg_4Nb_2O_9$	Hexagonal	23

The increase in the reinforcement of about 6% Nb_2O_5 + AZ31 has a different morphology compared to 3% Nb_2O_5 + AZ31, as shown in the SEM image of Figure 4. Further addition of reinforcement led to oxygen agglomeration, specifically in the grain boundary. Zinc and niobium correspond to Figure 4d,e with a uniform distribution, despite the fact that aluminum with an agglomerative character formed $Mg_{17}Al_{12}$, as reported by B.R. Sunil et al. [14] and following the same as shown in pure AZ31 and 3% Nb_2O_5 + AZ31.

3.1.2. XRD-Analysis and Phase Quantification

In Figure 5, the phase composition of Nb_2O_5/AZ31 composite samples was examined by XRD analysis. The XRD data shows a high intensity of α-Mg at (1 0 1) and a closely related quasicrystal line $Al_5Mg_{11}Zn_4$, which has an orthorhombic crystal structure instead of hexagonal due to distortion [15]. At approximately 36 degrees (in 2θ degree) $Mg_{17}Al_{12}$ at (4 1 1), and at 37 degrees β-Al_3Mg_2 at (11 3 3) were traced. The reason for the formation of β-Al_3Mg_2 was continuous heating after 723 K and usually pure β-Al_3Mg_2 was left after this temperature [16]. Though the percentage of these two secondary phases was considerably less i.e., 0.8%, 0.6%, and 0.5% of $Mg_{17}Al_{12}$ in pure AZ31, 3% Nb_2O_5/AZ31, and 6% Nb_2O_5/AZ31. Al_3Mg_2 formed in pure AZ31, 3% Nb_2O_5/AZ31, and 6% Nb_2O_5/AZ31 was 6.2%, 4.3%, and 5.6%. Another phase with a hexagonal crystal structure was obtained, i.e., $Mg_4Nb_2O_9$, which, according to K. Sarkar, V. Kumar, Shashank Bhushan Das et al., has a high band gap with low dielectric loss and excellent photoluminescence [17].

The effective reduction in grain size is shown in Figure 6, and a little variation can be observed in the microstrain and dislocation density in Figures 7 and 8. The trace of secondary β-$Al_{12}Mg_{17}$ was found in all the compositions, but the uniformness in the distribution of the discontinuous secondary phase increased with the addition of reinforcement. The proper distribution of the secondary phase and the less agglomeration of aluminum precipitate in 3% Nb_2O_5 reduced the local inhomogeneity along the grain boundary [4]. However, a reduction in microstrain can be due to a reduction in dislocation density, as stated by R.S. Lei et al. [18]. The orthorhombic phase of $Al_5Mg_{11}Zn_4$ belongs to the quasicrystalline [19]. The orthorhombic phase has the valuable quality of storing energy [20], which might be because of its non-periodicity. Hydrogen absorption and desorption might be tested in the future.

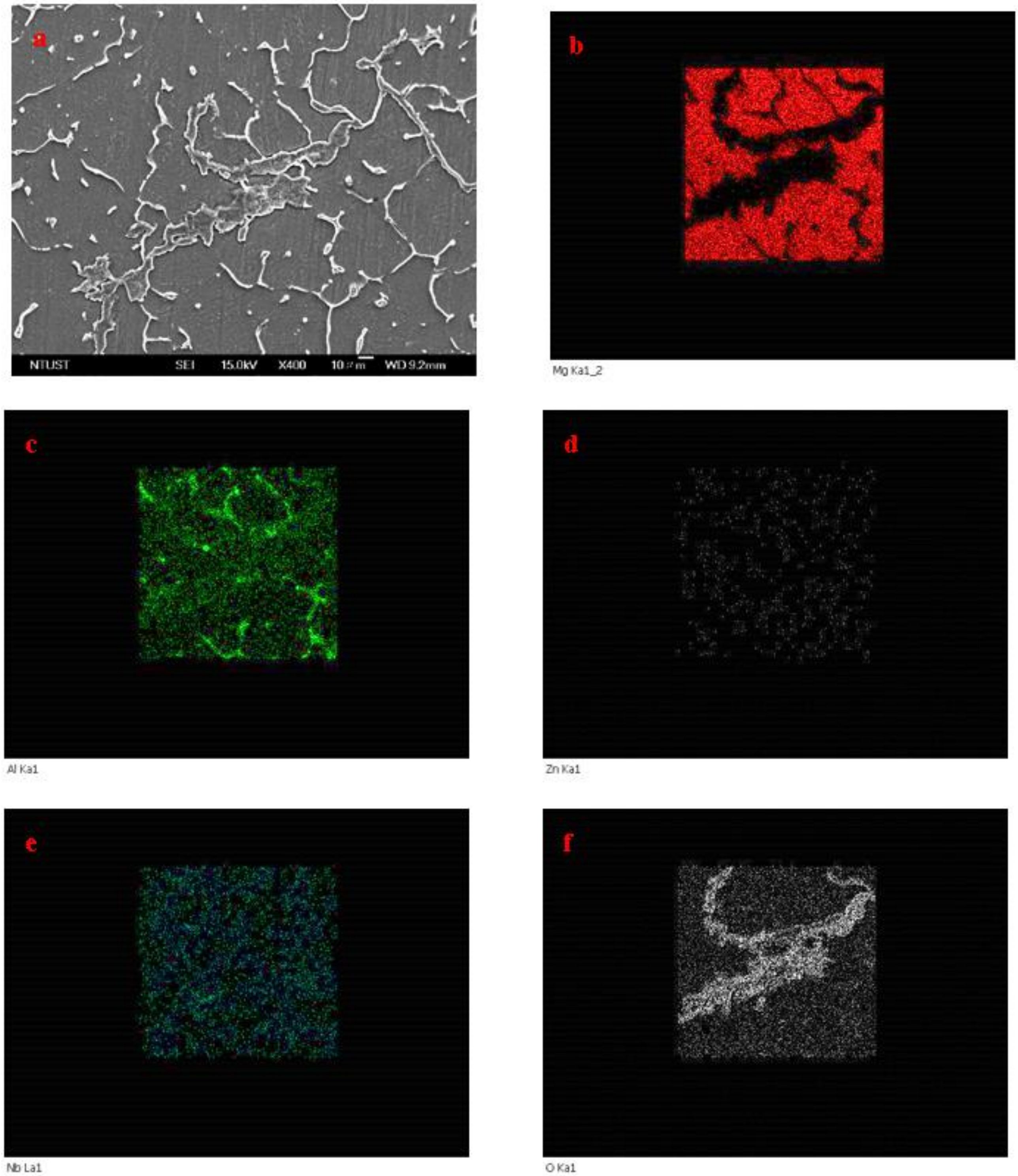

Figure 4. (**a**) SEM image of 6% Nb_2O_5 + AZ31 microstructure, (**b**) EDS shows Mg distribution, (**c**) EDS shows Al distribution, (**d**) EDS shows Zn distribution, (**e**) EDS shows Nb distribution, (**f**) EDS shows O distribution.

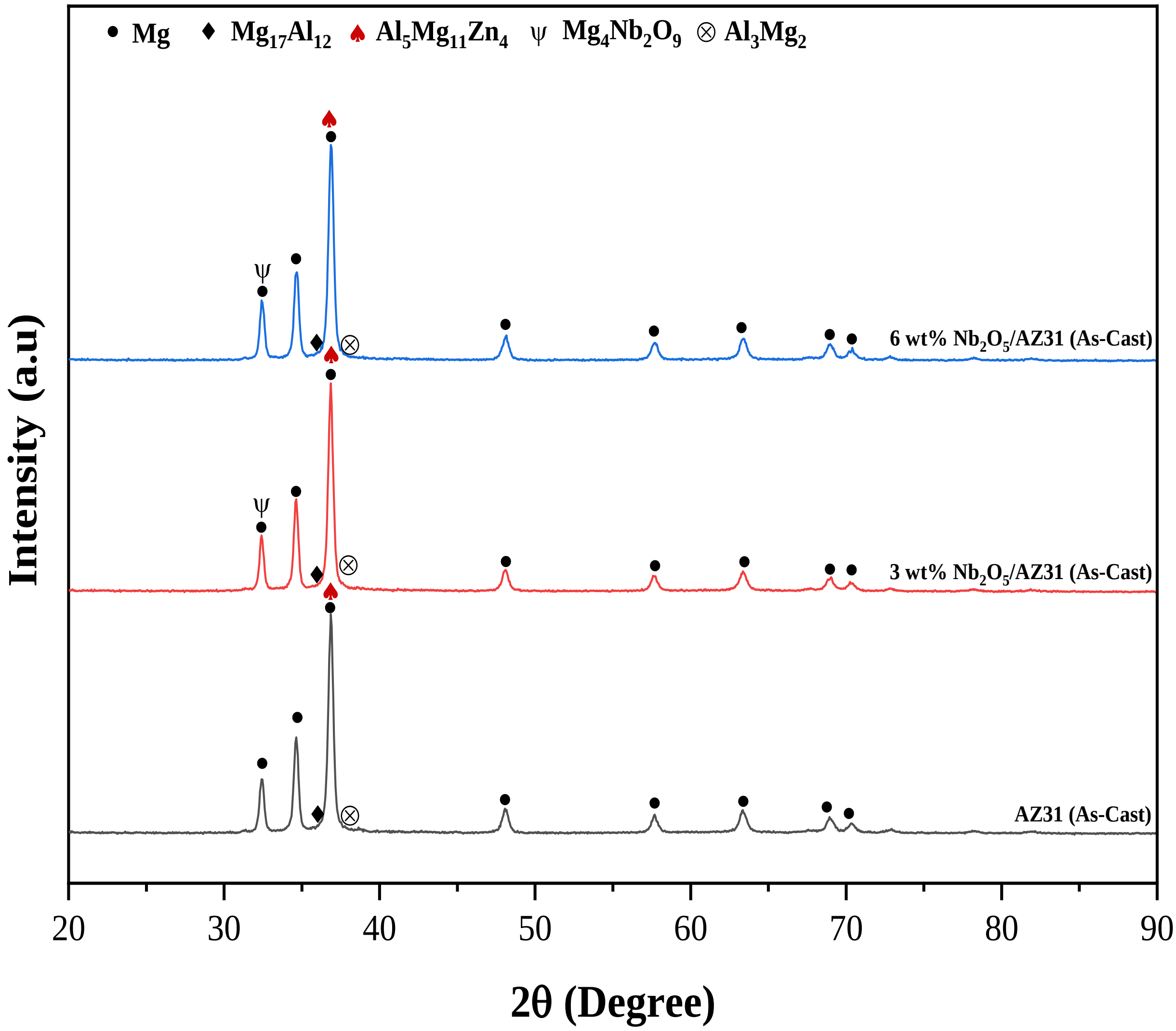

Figure 5. XRD shows the intensity of different phase compositions.

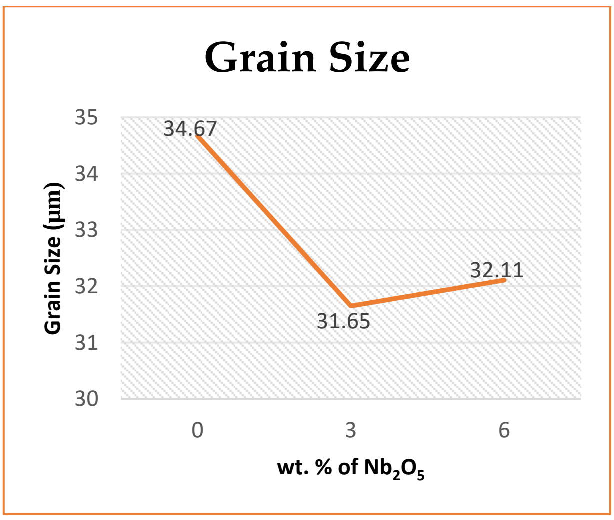

Figure 6. The graph shows the grain size.

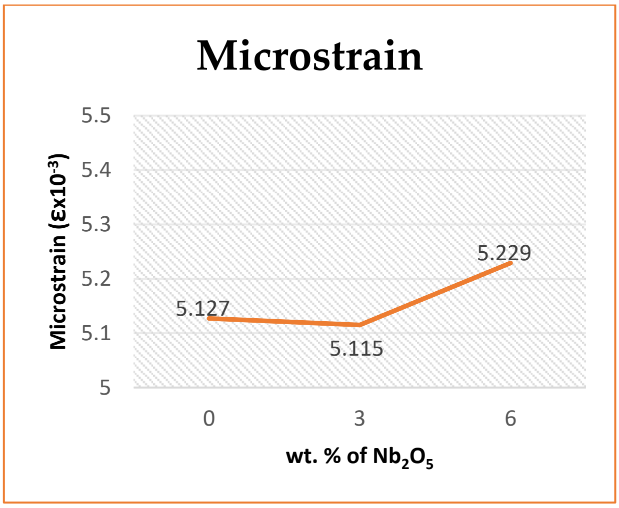

Figure 7. The grain shows the microstrain.

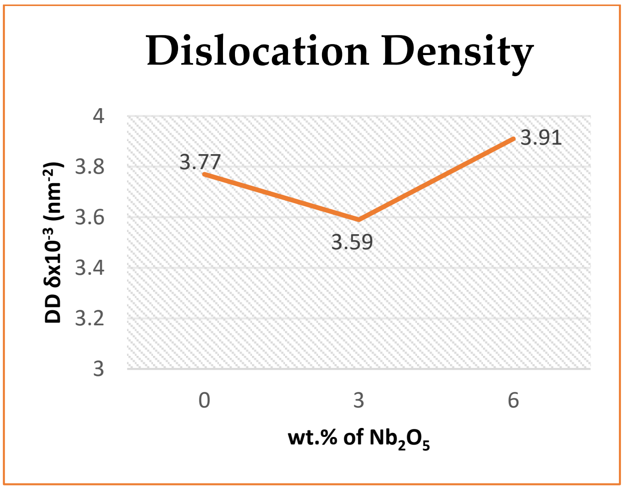

Figure 8. The graph shows the dislocation density.

3.2. Compression and Microhardness

Figure 9 shows the compressive load-bearing capacity and the relative change in length. The peak compressive stress of 323.25 MPa and fracture strain of 24.09% show the progress in Table 3, the composite has an increment of 18.68% for 3% Nb_2O_5/AZ31 and 9.15% for 6% Nb_2O_5/AZ31 when compared with pure AZ31. The compressive strain value had an improvement of 6.17% for 3% Nb_2O_5 and 11.28% for 6% Nb_2O_5 compared to pure AZ31. The curve shows a small enhanced compressibility property compared to the pre-compression analyzed by H. Zhang et al. [21]. The slope in the curve shows that the increase in stress and strain seems proportional to a much larger distance for 3% Nb_2O_5/AZ31 compared to pure AZ31 because of the reinforcement.

Table 3. Shows peak stress, fracture strain, and microhardness.

Composite	Ultimate Compressive Strength (MPa)	Strain (%)	Microhardness (HV)
Pure AZ31	272.36	22.69	55.06 ± 7.56
3 wt.% Nb_2O_5/AZ31	323.25	24.09	58.68 ± 2.85
6 wt.% Nb_2O_5/AZ31	297.23	25.25	59.68 ± 5.13

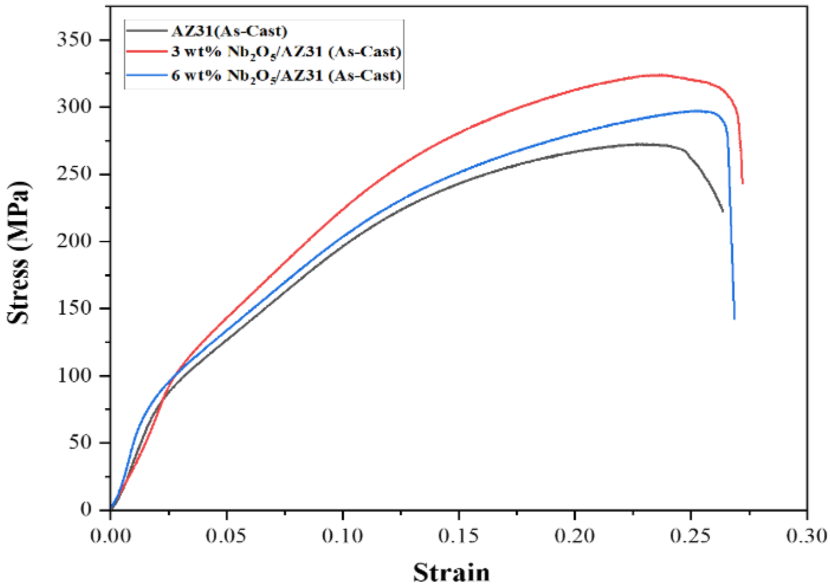

Figure 9. Compressive strength of Nb_2O_5/AZ31 composites.

The microhardness shown in Table 3 explains that the addition of reinforcement increases the microhardness by 6.57% for 3% Nb_2O_5 compared to monolithic AZ31. However, the increment percent slows down for further addition of Nb_2O_5 because for 6% Nb_2O_5, the increment is just 1.7% compared to 3% Nb_2O_5. The increase in hardness shows a decrease in intermetallic partial spacing for reinforced AZ31 compared to pure AZ31 [22] and also because of the hard ceramic particles (Nb_2O_5) present in the matrix, the composite exhibits a greater microhardness due to the high constraint on matrix deformation during indentation.

3.3. Fractography

The SEM image of the fracture surface obtained after the compression test shows various morphologies for different compositions.

3.3.1. Fracture Study of AZ31

The fracture surface morphology of AZ31 is shown in Figure 10. The secondary phase $Mg_{17}Al_{12}$ agglomerated impurity can be seen on the surface which has a clean surface morphology. The surface was debonded easily, which could be the reason for crack initiation. Some observable microcracks show initiation from the secondary phase flakes. Though the twins can be observed in the enlarged view the percentage is not much.

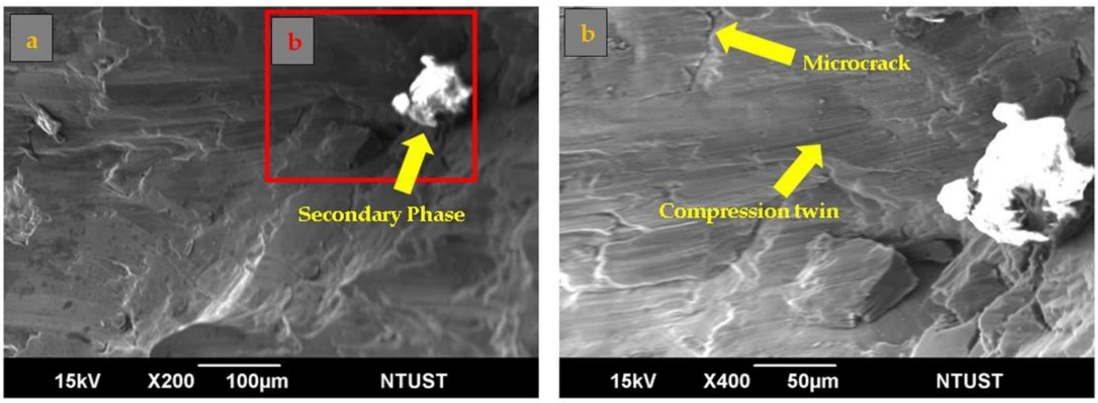

Figure 10. (**a**) The fracture surface morphology of pure AZ31. (**b**) Magnified inset section of figure (**a**).

3.3.2. Fracture Study of 3% Nb_2O_5 + AZ31

The fracture surface morphology of 3% Nb_2O_5 + AZ31 is shown in Figure 11. The reinforcement shows an improvement in the fracture surface with fewer microcracks with basal slip and compression twin. Adiabatic shear bands (ASB) can be seen because of the high-stress concentration due to compression [23]. The low grain boundary diffusion of magnesium, along with compression stress, forms the white bands called ASB. The addition of Nb_2O_5-induced inclusion can be seen in the basal slip surface.

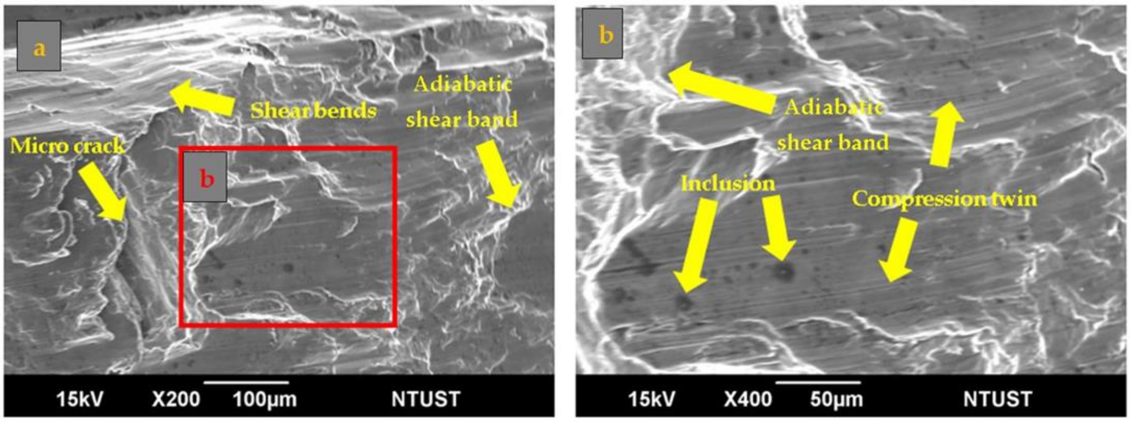

Figure 11. (**a**) The fracture surface morphology of 3% Nb_2O_5 + AZ31. (**b**) Magnified fracture surface of figure (**a**).

3.3.3. Fracture Study of 6% Nb_2O_5 + AZ31

The fracture surface morphology of 6% Nb_2O_5 + AZ31 is shown in Figure 12. The agglomeration of reinforcement and secondary phase can be seen with the formation of micropores. The enlarged view has no trace of extension twining but many adiabatic shear bands can be seen. The microcrack and shear band initiated from local stress developed by the agglomerated aluminum precipitate in the grain boundary leads to the reduction in peak compression stress.

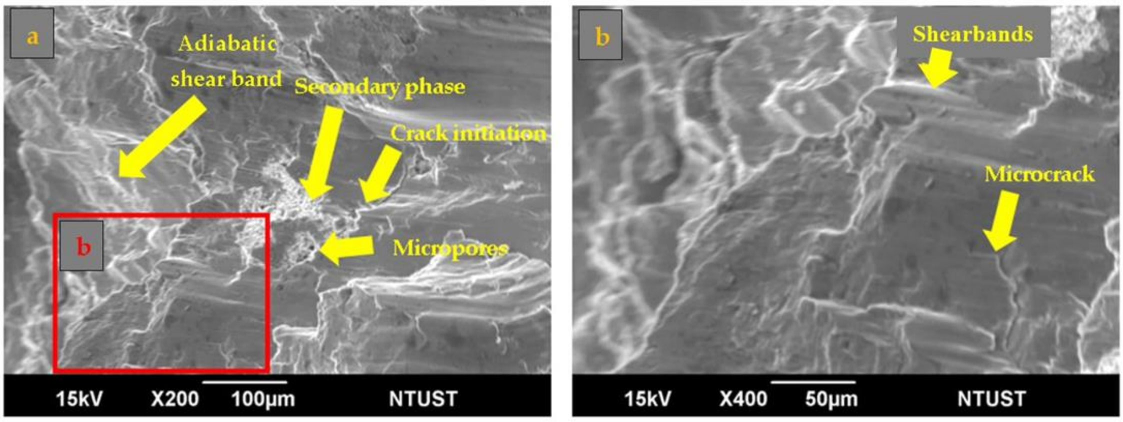

Figure 12. (**a**) The fracture surface morphology of 6% Nb_2O_5 + AZ31. (**b**) Magnified inset fracture surface of figure (**a**).

4. Conclusions

The Nb_2O_5/AZ31 composite shows an improvement in its properties, which can be concluded as follows:

- Although there is no shift in plane obtained, the addition of reinforcement distributes the secondary phase evenly throughout the matrix, which reduces the local inhomo-

geneity in the case of 3% Nb_2O_5. Furthermore, an improvement in grain size reduction was observed.
- The compression stress–strain curve reviled that the stress endurance increased by 18.68% for 3% Nb_2O_5 reinforcement with peak stress of 323.25 MPa. However, in the case of microhardness, the increment was 6.5% (3% Nb_2O_5) and 8.3% (6% Nb_2O_5) compared to the AZ31 composite.
- The fracture analyses show maximum basal slip in AZ31 and 6% Nb_2O_5 + AZ31, but 3% Nb_2O_5 shows much more ASB, which indicates the resistance towards the applied stress.

Author Contributions: Validation, writing—review, editing, supervision, formal analysis S.-J.H.; Conceptualization, methodology, writing—original draft preparation, S.K. and M.S. All authors have read and agreed to the published version of the manuscript.

Funding: The authors would like to thank the Ministry of Science and Technology, Taiwan (MOST 111-2221-E-011-096-MY3) for providing financial support.

Conflicts of Interest: The authors declare no conflict of interest.

References

1. Song, J.; Chen, J.; Xiong, X.; Peng, X.; Chen, D.; Pan, F. Research Advances of Magnesium and Magnesium Alloys Worldwide in 2021. *J. Magnes. Alloys* **2022**, *10*, 863–898. [CrossRef]
2. Aghion, E.; Bronn, B.; Eliezer, D. The Role of the Magnesium Industry in Protecting the Environment. *J. Mater. Process. Technol.* **2001**, *117*, 381–385. [CrossRef]
3. Huang, S.J.; Mose, M.P.; Kannaiyan, S. Artificial Intelligence Application in Solid State Mg-Based Hydrogen Energy Storage. *J. Compos. Sci.* **2021**, *5*, 145. [CrossRef]
4. Huang, S.J.; Ali, A.N. Effects of Heat Treatment on the Microstructure and Microplastic Deformation Behavior of SiC Particles Reinforced AZ61 Magnesium Metal Matrix Composite. *Mater. Sci. Eng. A* **2018**, *711*, 670–682. [CrossRef]
5. Huang, S.J.; Subramani, M.; Borodianskiy, K. Strength and Ductility Enhancement of AZ61/Al2O3/SiC Hybrid Composite by ECAP Processing. *Mater. Today Commun.* **2022**, *31*, 103261. [CrossRef]
6. Subramani, M.; Huang, S.J.; Borodianskiy, K. Effect of SiC Nanoparticles on AZ31 Magnesium Alloy. *Materials* **2022**, *15*, 1004. [CrossRef]
7. Huang, S.-J.; Subramani, M.; Chiang, C.-C. Effect of Hybrid Reinforcement on Microstructure and Mechanical Properties of AZ61 Magnesium Alloy Processed by Stir Casting Method. *Compos. Commun.* **2021**, *25*, 100772. [CrossRef]
8. Subramani, M.; Huang, S.J.; Borodianskiy, K. Effect of WS2 Nanotubes on the Mechanical and Wear Behaviors of AZ31 Stir Casted Magnesium Metal Matrix Composites. *J. Compos. Sci.* **2022**, *6*, 182. [CrossRef]
9. Abbas, A.; Huang, S.J. Investigating the Hall-Petch Constants for as-Cast and Aged Az61/Cnts Metal Matrix Composites and Their Role on Superposition Law Exponent. *J. Compos. Sci.* **2021**, *5*, 103. [CrossRef]
10. Abbas, A.; Huang, S.J. Investigation of Severe Plastic Deformation Effects on Microstructure and Mechanical Properties of WS2/AZ91 Magnesium Metal Matrix Composites. *Mater. Sci. Eng. A* **2020**, *780*, 139211. [CrossRef]
11. Song-Jeng, S.K.; Huang, M.S. Effect of Nano-Nb2O5 on the Microstructure and Mechanical Properties of AZ31 Alloy Matrix Nanocomposites. *Adv. Nano Res.* **2022**, *13*, 407–416. [CrossRef]
12. Zhu, J.; Yang, W.; Yang, H.; Wang, F. Effect of Nb2O5 on the Microstructure and Mechanical Properties of TiAl Based Composites Produced by Hot Pressing. *Mater. Sci. Eng. A* **2011**, *528*, 6642–6646. [CrossRef]
13. Safavi, M.S.; Walsh, F.C.; Visai, L.; Khalil-Allafi, J. Progress in Niobium Oxide-Containing Coatings for Biomedical Applications: A Critical Review. *ACS Omega* **2022**, *7*, 9088–9107. [CrossRef]
14. Sunil, B.R.; Ganesh, K.V.; Pavan, P.; Vadapalli, G.; Swarnalatha, C.; Swapna, P.; Bindukumar, P.; Pradeep Kumar Reddy, G. Effect of Aluminum Content on Machining Characteristics of AZ31 and AZ91 Magnesium Alloys during Drilling. *J. Magnes. Alloys* **2016**, *4*, 15–21. [CrossRef]
15. Nie, J.F. Precipitation and Hardening in Magnesium Alloys. *Metall. Mater. Trans. A* **2012**, *43*, 3891–3939. [CrossRef]
16. Zhou, Y.; Zhu, Y.; Zhu, Y.; Li, L. Phase Transformation, Kinetics and Thermodynamics during the Combustion Synthesis of Mg2Al3 Alloy. *J. Alloys Compd.* **2015**, *628*, 257–262. [CrossRef]
17. Sarkar, K.; Kumar, V.; Das, S.B.; Kumar, M.; Manash, A.; Biswas, C.; Mukherjee, S. Studies of Structural, Electrical and Optical Properties of MgNb2O6-Mg4Nb2O9nanocomposite for Possible Opto-Electronic Applications. In *Proceedings of the Materials Today: Proceedings*; Elsevier Ltd.: Amsterdam, The Netherlands, 2021; Volume 44, pp. 2459–2465.
18. Lei, R.S.; Wang, M.P.; Li, Z.; Wei, H.G.; Yang, W.C.; Jia, Y.L.; Gong, S. Structure Evolution and Solid Solubility Extension of Copper-Niobium Powders during Mechanical Alloying. *Mater. Sci. Eng. A* **2011**, *528*, 4475–4481. [CrossRef]
19. Singh, A.; Rosalie, J.M.; Somekawa, H.; Mukai, T. Crystallographic Relationship of Orthorhombic φ-Al5Mg 11Zn4 Phase to Icosahedral Quasicrystalline Phase. *J. Alloys Compd.* **2011**, *509*, 4676–4681. [CrossRef]

20. Manuja, M.; Thomas, T.; John, S.; Jose, J.; Jose, G. Electrochemical Characterization of Orthorhombic Tungsten Trioxide Hydrate for Battery Applications. *J. Alloys Compd.* **2021**, *869*, 159234. [CrossRef]
21. Zhang, H.; Bai, X.; Hou, M.; Wang, L.; Zhang, Q.; Fan, J.; Wu, Y.; Dong, H.; Xu, B. Enhancing Compressive Mechanical Properties of Rolled AZ31 Mg Alloy Plates by Pre-Compression. *Mater. Sci. Eng. A* **2020**, *772*, 138686. [CrossRef]
22. Paramsothy, M.; Hassan, S.F.; Srikanth, N.; Gupta, M. Enhancement of Compressive Strength and Failure Strain in AZ31 Magnesium Alloy. *J. Alloys Compd.* **2009**, *482*, 73–80. [CrossRef]
23. Malik, A.; Wang, Y.; Cheng, H.; Khan, M.A.; Nazeer, F.; An, R.; Bao, J.; Wang, M. Fracture Behavior of Twin Induced Ultra-Fine Grained ZK61 Magnesium Alloy under High Strain Rate Compression. *J. Mater. Res. Technol.* **2019**, *8*, 3475–3486. [CrossRef]